Available online at www.sciencedirect.com
SCIENCE DIRECT
Wear 260 (2006) 580–593
WEAR
www.elsevier.com/locate/wear

In situ wear studies of surface micromachined interfaces subject to controlled loading

Erin E. Flater [a], Alex D. Corwin [b], Maarten P. de Boer [b], Robert W. Carpick [a,*]

[a] *Department of Engineering Physics, University of Wisconsin-Madison, Madison, WI 53706, USA*
[b] *Reliability Physics Department, Sandia National Laboratories, Albuquerque, NM 87185, USA*

Received 13 July 2004; received in revised form 29 December 2004; accepted 7 February 2005
Available online 19 March 2005

Abstract

Friction and wear are major limiting factors for the development and commercial implementation of devices fabricated by surface micromachining techniques. These tribological properties are studied using a polycrystalline silicon nanotractor device, which provides abundant, quantitative information about friction and wear at an actual microelectromechanical system (MEMS) interface. This in situ approach to measuring tribological properties of MEMS, combined with high-resolution atomic force microscope (AFM) images of wear tracks, provides insight into the effects of different MEMS surface processing on wear. In particular, monolayer coatings have a significant positive effect, while surface texturing does not strongly affect performance.

Keywords: Microscale wear; Microelectromechanical systems (MEMS) reliability; Nanotractor; Monolayer coatings; Polycrystalline silicon; Atomic force microscopy (AFM)

1. Introduction

Microelectromechanical systems (MEMS) have received much attention in recent years, due to their promise as the mechanical counterpart to integrated circuit technologies. Success of MEMS would allow for substantial technological advances in the automotive and telecommunications industries and in the area of national defense. Devices with no contacting components, such as airbag accelerometers [1] and pressure sensors [2], have been successfully marketed. Micromirror arrays for overhead projectors [3,4] are the only commercialized devices to date that allow adhesive contact between components. Many MEMS device concepts, such as microengines and their associated components, including gears, guides, linear racks, and pop-up mirrors [5,6], torsional ratcheting actuators [7], wedge stepper motors [8], and stepper motors [9], require not only contact between surfaces, but relative sliding of these surfaces.

MEMS devices are commonly fabricated by a process known as surface micromachining, which leverages the integrated circuit fabrication toolset. Prototype devices consisting of five structural levels can be constructed [10], and commercial devices can also be produced in high volume applications [1]. Polycrystalline silicon (polysilicon) is often used as the structural material in surface micromachining because its material properties have been optimized in many respects. For example, very low residual stress levels (<10 MPa) [11,12] and low stress gradients (<0.2 MPa/μm) [11,13] are routinely achieved. Also, although polysilicon is brittle with a microstructure-independent fracture toughness of 1.0 MPa $m^{1/2}$ [14], it exhibits high strength (∼2–5 GPa) [14,15]. In practice, strength and fatigue-related failures are not observed because flexure is due to bending stresses in very thin and narrow beams, resulting in very low applied stresses compared to the fracture strength. For example, billions of cycles without failure have been demonstrated in an optical switch application [16]. However, because of high surface-to-volume ratios at the microscale compared to the macroscale, tribo-

* Corresponding author. Fax: +1 608 263 7451.
E-mail address: carpick@engr.wisc.edu (R.W. Carpick).

0043-1648/$ – see front matter © 2005 Elsevier B.V. All rights reserved.
doi:10.1016/j.wear.2005.02.070

logical issues including adhesion, friction, and wear become critical.

These issues have been highlighted in several different investigations. One of the earliest surface-micromachined actuators was a microturbine driven by gas flow from a micropipette [17], which highlighted the severe tribology issues that can occur at this scale. After fabrication, the sacrificial material around the structural material was removed by a wet chemical etchant, which was then displaced by water. The devices were air-dried and the associated capillary forces would cause the surfaces to adhere strongly. These devices could be freed by mechanical probing, and they would then work for a limited time. A dynamic friction coefficient of 0.28 was estimated by a deceleration measurement. Operation was limited to about one million cycles at 5000 revolutions per second (∼0.3 m/s with a 20 μm diameter hub) due to wear as limited by run-out of the hub (under unknown loading conditions) [18].

An electrostatic micromotor, driven by phased voltages applied at stators, was also developed at about the same time [19]. From the equations of motion (with the positional dependence of torque calculated from electrostatic simulation) and by comparing to experimental results from video microscopy, the dynamic friction coefficient of the polysilicon in contact with silicon nitride was estimated at between 0.2 and 0.38 [20]. This motor endured for up to 1 min at five revolutions per second before failure.

In these micromotor studies, the apparent applied pressures are not known because small tilts in the device change the area of contact from two parallel surfaces to a line contact with much higher pressures. Lim et al. [21] developed a friction test structure based on a single electrostatic comb drive and a friction foot to which electrostatic voltages could be applied to controllably vary the load. Even though the rubbing surfaces were nominally the same as in the wobble motor, a static coefficient of friction of approximately 5 was measured.

Beerschwinger and colleagues developed specimen-on-disc samples with controlled areas of contact [22]. They coated these samples with various micromachining-compatible materials and measured the friction and wear properties at the same pressures as those calculated in their micromotors. They found that for low nominal contact pressures the wear rate settled into a constant value independent of pressure, but for higher pressures wear rates were similar to that predicted for macroscale contacts. Although their motors did not function well, their calculations, based on measured friction values, indicated the addition of a bushing and a more symmetric stator design would result in working devices [23].

Improved processing techniques to address these tribology issues have been reported. A critical point drying process, which avoids the capillary problem after release, has been developed [24]. Also, processes for depositing organic monolayer lubricants by liquid [25,26] and vapor [27] deposition routes have been developed. These processes all result in much higher yield of micromachined devices, while the monolayers reduce the friction coefficient to as low as ∼0.1.

In a significant enhancement to the micromotor concept, Sniegowski and Garcia [28] reported a design and process for a microengine that allowed a small gear driven by orthogonal electrostatic comb drives to be rotated via a pin linkage and to couple to other gears. Miller et al. [29] derived the microengine equations of motion and demonstrated that over one billion cycles could be achieved before failure if optimized signals were applied. On the other hand, by operating the device near resonance (3 kHz), Tanner and Dugger found that the device could fail in as few as 100,000 cycles [30]. In their study, microengines and friction test devices were fabricated, and the lifetime and wear of the monolayer-coated microengines compared to friction and wear of the test devices [30]. The failure analysis showed that the debris generated by both devices was an agglomerated silicon oxide. However, much more debris was generated at a low humidity (1%) in the microengine than in the friction test structure, whereas at high humidity (40%) more debris was generated in the test structure than in the microengine. These differences were attributed to differences in the operating speeds, operating pressures and the degree of debris trapping of the two devices.

Indentation testing on silicon [31], as well as scratch testing [32] and atomic force microscopy (AFM) testing [33] on silicon, doped and undoped polysilicon and silicon carbide have been reported. While these studies were not performed on micromachined devices and therefore do not necessarily reflect details of the processing or actual loading conditions, they do give information on the material deformation mechanisms. It has been demonstrated that silicon deforms plastically by undergoing transitions to crystalline and amorphous phases [31]. Similarly, n+ polysilicon appears to deform in a ductile fashion under scratching conditions [32,33]. This material behavior is possible because high shear stresses can develop in the hydrostatic compressive field under the indenter and scratch tips.

In both the micromotors and the microengine, and also in many other devices where the design allows contacting surfaces, friction is a detrimental effect. Also, it is difficult to know the pressure distribution in detail in these devices. In contrast, the nanotractor[1] design studied here takes advantage of friction to obtain high-performance characteristics such as nanometer-scale step size for precision alignment, a large in-plane actuation force (0.5 mN) and a large travel distance (±100 μm) [34]. Furthermore, the same actuator is also a model friction test structure with well-known normal loads from 1 μN [35] to 10 mN [34]. Changes in friction and wear must be understood to ensure that the actuator performance is predictable. Because the actuator and the test structure are integrated into the same device, it is more likely that friction

[1] This actuator was previously called an “inchworm” in refs. [34,35]. The “Inchworm®” trademark is owned by EXFO Burleigh Products Group Inc in the field of electromechanical actuators.

and wear measurements will lead to an understanding of its failure mechanisms than was possible in the studies reported above, since the measurements are taken during actual nanotractor operation.

Based on these considerations, we report here an initial wear study of wear in the nanotractor. Information about induced surface wear is obtained using high-resolution AFM images of worn polysilicon surfaces, which show that wear can be produced in a controlled fashion. Our results also indicate that wear performance is strongly improved by the presence of a monolayer coating while at the same time, it is not yet clear whether surface roughness has any effect on the tribological behavior of these surfaces.

2. Background information on the nanotractor

The nanotractor is a recently-developed tool for understanding friction and wear for MEMS devices [34]. Its design has been previously discussed in detail [34] and is briefly reviewed here. Fig. 1 shows how motion of the nanotractor is achieved by sequentially actuating and releasing the central driving plate while the clamps are alternately held in place using electrostatic potentials. The actuation plate electrode is segmented by electrically grounded standoffs, as shown in the figure, that prevent electrical shorting of the plate to the plate electrode and establish amplitude A. Using a phased sequence of voltages, as shown in Fig. 2, the nanotractor can travel $\pm 100\ \mu m$ in 50 nm steps.

A scanning electron microscope (SEM) image of a nanotractor is shown in Fig. 3(a). A schematic cross-section through the dashed line YY′, shown in Fig. 3(b), illustrates the design of the nanotractor clamp and actuation plate. The device, consisting of five layers of polysilicon, is made using the SUMMiT V^{TM} process developed at Sandia National

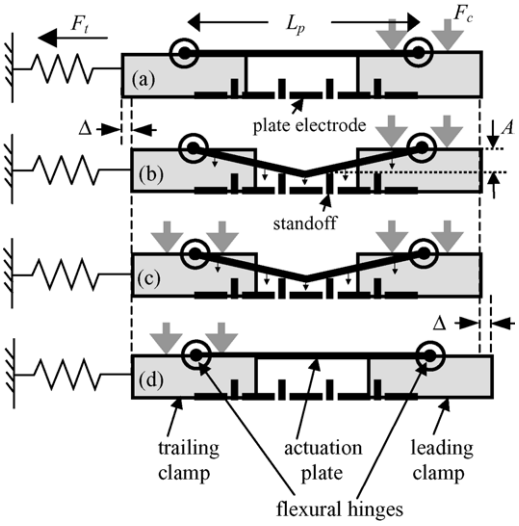

Fig. 1. Nanotractor schematic with signals applied to achieve rightward motion. The actuation plate electrode is segmented by electrically grounded standoffs that prevent electrical shorting and establish amplitude A.

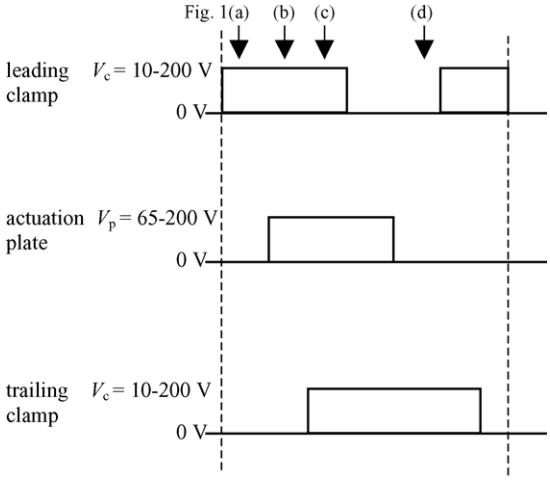

Fig. 2. Timing diagram (right) for Fig. 1 (one cycle). Voltage ranges indicate levels over which the device typically operates. The signals are shown to achieve one step of walking to the right. To walk to the left, the signals to the clamps are interchanged, and the left (right) clamp becomes the leading (trailing) clamp.

Laboratories [10]. The labeling convention on the right side of Fig. 3(b) denotes each polysilicon layer, starting from P0 at the bottom and continuing to P4 at the top. During the construction process, sacrificial oxide layers (denoted SO1, SO2, etc.) are deposited between these layers to control the polysilicon layer separations and are later removed in a "release etch" to create free-standing structures as shown in Fig. 3(a). Fig. 3(c) is a close-up SEM of a focused ion beam milled cross-section to show the frictional counterfaces, which are nominally parallel. This region in Fig. 3(c) is indicated in Fig. 3(b) by the dotted oval. The P12 layer labeled in Fig. 3(c) is a hybrid layer of P1 and P2.

Fig. 3(b) shows in detail how the nanotractor is actuated and where contact is made during operation. Normal force is applied electrostatically by the clamp electrodes of width w_c, but is borne mechanically by the frictional counterfaces of width w_f. The experiments reported here were performed on nanotractors with two clamps each $L_c = 600\ \mu m$ long and frictional pads $w_f = 2\ \mu m$ wide on each side (see Fig. 3(b)) running the entire length of the clamps, for a total apparent contact area of $2400\ \mu m^2$ per clamp. In our discussions below, we use the term "apparent contact area" because the *true* contact area at this interface is determined by nanoscale surface asperities, and is much smaller than the apparent contact area.

The wear test, which will be described below, is used to deliberately induce wear on the nanotractor surfaces under controlled conditions. We must first determine what clamping force (F_c in Fig. 1) would be needed to induce surface wear during this test. The electrostatic clamping force exerted on an individual friction pad can be written to first order as:

$$F_c(V_c) = 2\varepsilon_0 w_c L_c \left(\frac{V_c}{g_c}\right)^2, \quad (1)$$

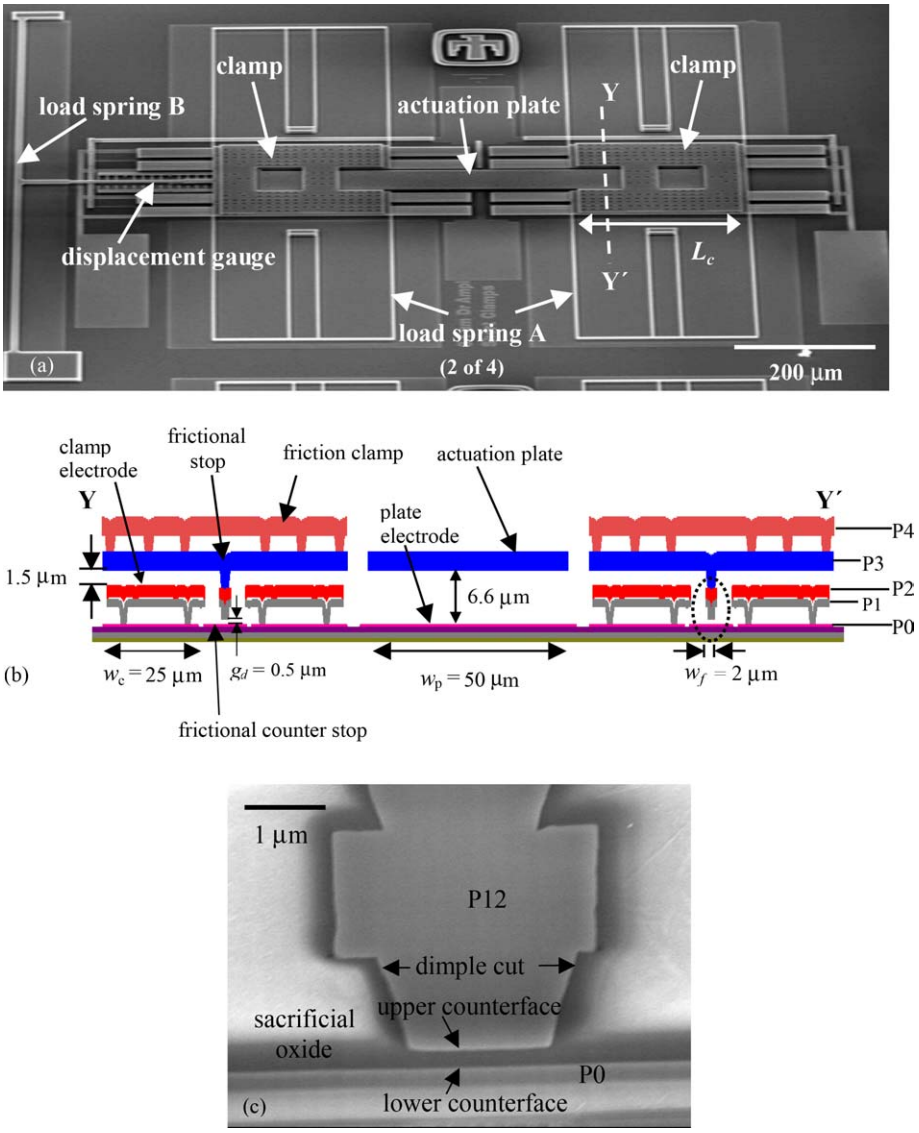

Fig. 3. (a) SEM image of the nanotractor (clamp length $L_c = 200$ μm). (b) Schematic cross-section at YY′ as indicated in (a) showing the friction clamps, the associated frictional stops and the actuation plate. Actuation is achieved via the plate and clamp electrodes. The actuation plate, friction clamp, frictional stop and its opposing counter stop are electrically grounded. The width direction is compressed $2\frac{1}{2}$ times relative to the height direction in this sketch. The circled area is shown in (c). (c) SEM image of a focused ion beam cross-section of the counterfaces. The surface is actually titled 45° with respect to the viewing plane, and is shown before the sacrificial oxide is etched from around the nanotractor. The upper counterface is formed by a dimple cut below P12, while the lower counterface is formed by P0. The counterfaces are nominally parallel.

where $\varepsilon_0 = 8.854 \times 10^{-12}(\text{Coulombs})^2 N^{-1}\text{m}^{-2}$ is the permittivity of free space (which is nearly the same as that of air), V_c is the clamping voltage applied between the plates, d is the distance between the clamp plates, $w_c = 25$ μm is the width of one of four clamp electrodes, and L_c is the length of the clamp (note that L_c shown in Fig. 3(a) is 200 μm; the clamps used in this study were 600 μm long). The gap distance $g_c = 1$ μm (referring to Fig. 3(b), $g_c = 1.5$ μm $- g_d$) applies when the friction pad is in contact, and the maximum V_c for the experimental setup used is 150 V. Therefore, each clamp can exert a maximum normal force of approximately 6 mN, which corresponds to a nominal (apparent) pressure of 2.5 MPa. In the wear tests, we chose $V_c = 20$ V because the corresponding load of 106 μN is the main contributor to the normal load. At this value, it is much larger than other loads that we cannot control such as the reaction force at the flexural hinges (worst case ∼30 μN), the adhesive force between the counterfaces (4.5 μN) [35], the out-of-plane force due to load spring A (−0.3 μN) and gravity (0.03 μN). Also, at slightly higher values of V_c (e.g., 30 V), the nanotractor would not travel in the wear tests described because the frictional resistance to sliding is too high. Therefore, we chose a reasonably high value of V_c anticipating that even though this pressure is low compared to other prototype MEMS devices that allow sliding, we would indeed observe wear. The apparent pressure is approximately 44 kPa for $V_c = 20$ V.

For comparison, the apparent pressure in practical MEMS devices of course depends on the geometry and the loads applied. For example, the internal radius of a hub in a typical MEMS microengine [28] is approximately 7.7 μm while the external radius is about 8 μm. Using the formula for two smooth cylinders in internal contact [36], the nominal pressure at a 1 μN load is ∼15 MPa. In fact, considering that there may be tilt changes between the contacting surfaces as the microgear rotates, the apparent pressure is not well controlled and may be considerably higher and these devices can exhibit severe wear [30]. On the other hand, the moment-induced pressure near an adhesive contact can be much lower. In this case, applying the calculation in ref. [37], the apparent pressure can be shown to be proportional to adhesion energy, and is ∼100 kPa for a nominal adhesion energy of 10 μJ/m^2. This is typical of an rf-MEMS relay switch where there would be no sliding, and in which wear is difficult to observe directly. As we shall see, although the nanotractor provides very useful actuation capability and controllable low apparent pressures, polysilicon material wear remains significant.

Two load springs restrict the motion of the nanotractor and are labeled “load spring A” and “load spring B” in Fig. 3(a), and nanotractors can be manufactured that are connected just to load spring A, or to both A and B. Restoring forces supplied by each of these load springs as a function of displacement from equilibrium are shown graphically in Fig. 4 [34]. Load spring A is a quartet of suspended joined W-shaped beams connecting the sides of the nanotractor to posts on the substrate. It is a weak, linear spring, as its restoring forces are negligible compared to load spring B when both are connected to the nanotractor. Load spring A consists of a fixed-guided geometry that serves to maintain linear motion and to electrically ground the nanotractor. Load spring B is a non-linear, strain-stiffening, fixed–fixed beam. Its non-linear behavior is useful since a large range of forces can be reached over a relatively small travel distance (approximately 20 μm). The nanotractor can ordinarily walk out a maximum distance of 20 μm when working against load spring B, for a maximum restoring force of about 450 μN, as seen from Fig. 4.

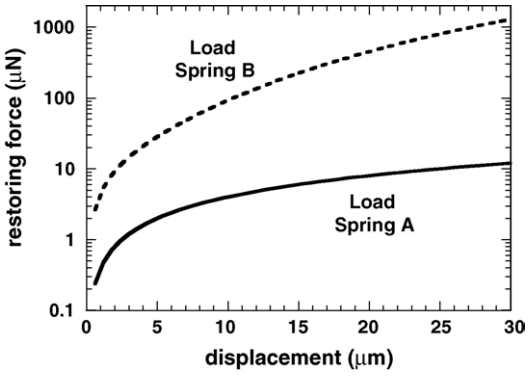

Fig. 4. Load-displacement curves of the load springs.

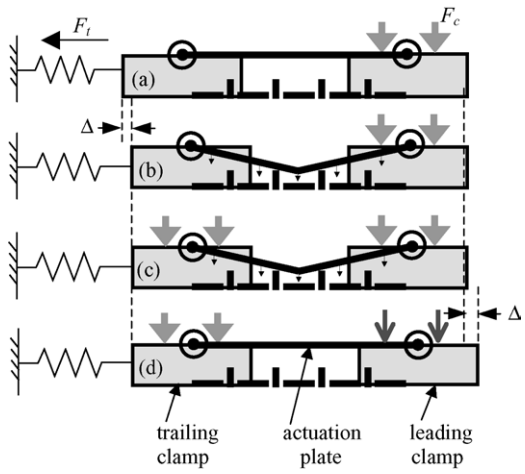

Fig. 5. Diagram of a nanotractor device with signals applied for one step to the right during a wear test. The clamping voltage applied to the leading clamp in (d) shows the only difference between this test and the regular walking mode of the nanotractor as in Fig. 1d. To walk to the left, the signals to the clamps are interchanged, but 20 V is maintained on the right (trailing) clamp so that wear takes place as the nanotractor is walked in either direction.

3. Tests performed

We conducted three types of tests on nanotractors that were manufactured with both load springs A and B connected to them. We refer to the first type as a “wear test”, which is represented schematically in Fig. 5. The sequence of voltages (forces) applied during one cycle of this test, which walks the nanotractor to the right, is shown in Fig. 6. Essentially this is the same as the normal walking sequence in Figs. 1 and 2, but now the leading clamp is subjected to an intentionally applied load F_c during the sliding step. This load is chosen to be high enough to enhance wear, but not too high to prevent sliding of the clamp. To perform this test, the nanotractor was walked back and forth 500 steps, keeping the load F_c applied to the leading clamp while it is pushed in sliding (i.e., in step (d) of Fig. 5). The leading clamp voltage used

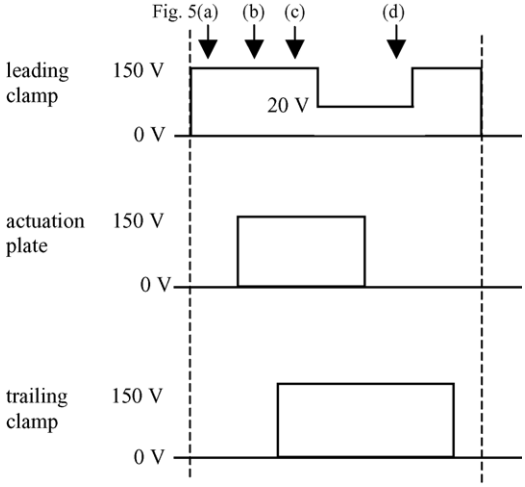

Fig. 6. Timing diagram for the wear test, as shown in Fig. 5 (one cycle).

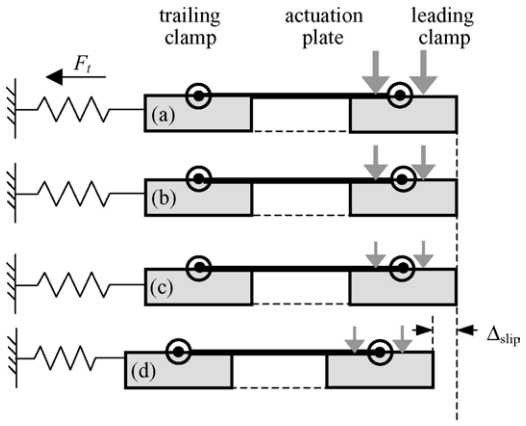

Fig. 7. Schematic diagram of the friction test. The nanotractor is first walked out to a large displacement in the manner of Figs. 1 and 2. Then the leading clamp is clamped as in (a). The load is gradually relaxed as in (b). In (c), as the normal load continues to relax, the force from load spring B overcomes the static friction force, and the nanotractor slides towards the equilibrium position of the load springs. In (d), after sliding a distance Δ_{slip}, the load spring force F_t has decreased below opposing tangential force components including the dynamic friction force, and the nanotractor comes to rest.

during sliding was 20 V, which according to Eq. (1) induces a normal clamping force of $F_c = 106\ \mu N$. To walk to the left, the signal sequence in Figs. 5 and 6 is effectively reversed. For this case, we maintain $V_c = 20$ V on the same clamp (which has become the trailing clamp), but now it is being pulled (i.e., like the trailing clamp in step (b)). The test is performed until the device fails. We define failure of a nanotractor for any test when the device does not move despite the repeated application of the usual actuation voltages.

The second test carried out, shown in Fig. 7, is a "friction test", which is used to determine the static force of friction for a range of normal loads. This can be used to determine the coefficient of friction. In a friction test, the nanotractor is first walked out 500 steps in the normal walking sequence shown in Figs. 1 and 2. When the nanotractor has completed the 500 steps and has reached the outermost position, 150 V (~6 mN) is applied to the leading clamp to hold it in place, while the trailing clamp and the beam are not actuated (Fig. 7(a)). This voltage on the leading clamp is then slowly reduced (Figs. 7(b) and (c)) until the restoring force on load spring B, F_t, overcomes the ever-decreasing static force of friction acting between the clamp and the substrate (Fig. 7(d)). The nanotractor then rapidly slides across the substrate, moving some distance Δ_{slip}, as shown in (d), and comes to rest again. V_c is reduced further, another sliding event occurs, and so on until V_c is zero. Assuming that friction varies linearly with normal load, the clamp will slip when $F_t \geq \mu_s F_N$, where μ_s is the coefficient of static friction. Therefore, we can obtain the static coefficient of friction at each slip location by dividing F_t by F_N for each slip event. For each friction test cycle, the nanotractor undergoes several slip events. There are approximately five or more slip events for initial test cycles, and as few as one or two when the surface has become more run-in.

In the third type of test, friction and wear tests are used in series to obtain further information about the tribological behavior of the nanotractor. We shall refer to this as a "friction and wear" test. For this procedure, the nanotractor is operated for a large number of wear cycles and then several friction tests are performed. This sequence is repeated until the device fails. This test is used to determine how the coefficient of friction changes as the surfaces are progressively worn.

The effect of wear on the nanotractor device can be analyzed in several ways. We chose to concentrate on two output parameters. First, the movement of the nanotractor was monitored using its travel distance as a measure of its performance with increasing numbers of wear cycles. Using a CCD camera and pattern recognition software, the position of the nanotractor is recorded after it walks out 500 steps, after it walks back 500 steps, and after all voltages on the clamps and plate are set to zero. The purpose of the final release of the clamps and plate is to bring the nanotractor back to the load springs' equilibrium position. Even so, the nanotractor may not return exactly to equilibrium when all voltages are zeroed due to surface adhesion, which creates a finite frictional resistance force even with no externally applied load. This position is recorded nonetheless to detect degradation of the nanotractor's performance as reflected in decreased or arrested travel.

The second method to evaluate the effect of wear is to directly measure the wear track topography using the AFM. Wear tracks were imaged using a Nanoscope IIIa Dimension 5000 AFM or a Nanoscope IV MultiMode AFM (Digital Instruments, Santa Barbara, CA), using intermittent-contact mode. With this technique, the AFM cantilever is oscillated at its resonant frequency and is allowed to lightly tap the sample surface. Topography is recorded as the tip scans, as well as the phase lag between the applied drive signal to the cantilever at its base and the resulting oscillation as the cantilever taps on the surface. This latter information is called the "phase" of the cantilever's oscillations and has a non-trivial relationship to the material damping, elastic parameters, tip shape, and interfacial forces between the surface and the cantilever. At the very least, the phase gives qualitative information about the response of the cantilever as it taps on a surface and is particularly useful for identifying material heterogeneity [39].

4. Process variations studied

For this paper, several nanotractor devices were studied, and the roughness and the lubricant coating were varied. These devices and their surface treatments are summarized in Table 1. Devices were selected from two different fabrication lots, "Lot A" and "Lot B". Four different variants of Lot A were examined. One involved no further surface treatment. Two involved increasing the roughness of the P0 layer by thermally oxidizing the P0 at 900 °C for 100 and 300 min, respectively, promoting uneven oxidation of grains depending on their orientation, followed by etching away this oxide

Table 1
Descriptions of the nanotractor samples tested, treatments applied to these samples, and number of cycles to failure

Lot	Wafer treatment	RMS roughness[a] (nm)	Coating	Cycles to failure
A	CMP	2.5 ± 0.5	FOTAS	7000
	Nominal	5.2 ± 0.5	FOTAS	8000
	100 min oxidation	7.1 ± 0.5	FOTAS	2700, 6800
	300 min oxidation	11.5 ± 1.0	FOTAS	5000, 6500
B	Nominal	4.0 ± 0.3	FOTAS	6000
	Nominal	4.5 ± 0.5	Oxide	2400, 4700

[a] RMS roughness was determined using 4 μm × 4 μm AFM images.

with HF leaving a rougher polysilicon surface that will then regain its native oxide due to ambient exposure. The fourth involved decreasing the roughness of the P0 layer by performing a chemical mechanical polishing step. At the end of the process flow, all wafers were released in HF:HCl acid to remove the sacrificial oxide layers, rinsed in water, oxidized in H_2O_2 at room temperature for 15 min and then processed with critical point drying with CO_2 as the working fluid [24] to obtain freestanding structures. They then received a perfluorinated monolayer lubricant coating (tridecafluoro-1,1,2,2-tetrahydrooctyl)tris(dimethylamino)-silane (chemical formula: $CF_3(CF_2)_5(CH_2)_2Si(N(CH_3)_2)_3$, abbreviation: FOTAS) [40].

Lot B was a separate lot that received only the nominal process flow, that is, no steps were taken to alter the roughness of the P0 layer. The subsequent release steps were identical. For this lot, two different final treatments were used. The nanotractor surfaces received either the critical point drying procedure alone, or the additional application of the FOTAS monolayer lubricant. We refer to the former surfaces as “oxide-coated”, because a thin oxide is grown during the exposure to H_2O_2. However, hydrocarbons or other contaminants may be adsorbed during the critical point drying procedure [41] or may physisorb before testing occurs. The latter surfaces with the FOTAS coating are referred to as “monolayer-coated”.

The root mean square (RMS) roughnesses of the P0 layer from each wafer and lot are indicated in Table 1. These values were calculated using 4 μm by 4 μm AFM images, taken on the Nanoscope IV MultiMode AFM. The uncertainty in these values reflects the range of roughness values depending on the region of the sample used for the calculation. In Lot A, the roughness of the P0 layer that received the nominal process flow was measured to be 5.2 nm RMS, while for Lot B it was 4.0–4.5 nm RMS. The roughness of the P0 layer resulting from the nominal process flow has been known to exhibit some lot-to-lot variation. These roughnesses are not affected by application of a monolayer, since this layer is conformal. Of course, the RMS roughness is only one measure of surface roughness. Although much more topographical characterization is warranted, we report only this value here. As well, we have observed via AFM that roughness in the P12 layer is affected by the roughness of the P0 layer. In a future paper, we will discuss in detail a multi-parameter characterization of MEMS surface topography.

5. Test results

5.1. Wear tests of the nanotractor device

Testing occurred within 2 months after the release and coating procedures described above were carried out. Before testing, the devices were stored in air (relative humidity about 30%) inside GelPak^{TM} containers. Environmental conditions during testing were similar (room temperature and relative humidity about 30%). Such conditions could be commonly encountered by a MEMS device.

Data from one representative wear test are shown in Fig. 8 on a Lot A device with CMP post-deposition processing of P0, i.e. the smoothest surfaces. Positions of the nanotractor in Fig. 8(a) were recorded after every tenth cycle during the wear test. First the nanotractor walks out 500 steps and its position is recorded (+500 position), which in Fig. 8(a) corresponds to a distance of 20.5 μm (ignoring the first transient point, which may simply reflect the influence of surface hydrocarbons that were removed during successive cycles). Next, the nanotractor walks back 500 steps and its position is recorded again (−500 position). Note that the nanotractor’s position changed by approximately 27.7 μm total, thus it has walked back further than it walked out. The clamp voltage is then released, and the nanotractor slides until it comes to rest, which initially is close to its starting position, and this position is again recorded (released position).

The discrepancy between the −500 position and the released position is due to constraint on the nanotractor’s motion by the nonlinear load spring B when at large distances from equilibrium. The restoring force acting on the nanotractor increases rapidly with distance from its equilibrium position (Fig. 4), reducing the nanotractor step size. This step size reduction can be attributed to stretching of the central plate [34]. Nanometer-scale slip of the leading clamp during the steps shown in Fig. 7(b) and (c) before the static friction limit is reached may also play a role [43]. In either case, the step size approaches zero as the nanotractor approaches the maximum force it can withstand from load spring B, approximately 0.5 mN.

During the first 2500 cycles, the nanotractor in Fig. 8(a) returns relatively close to its zero position after the release of voltages, but as the number of wear cycles increases, the nanotractor is less consistent in returning to this equilibrium position. In some instances (e.g., several such points around

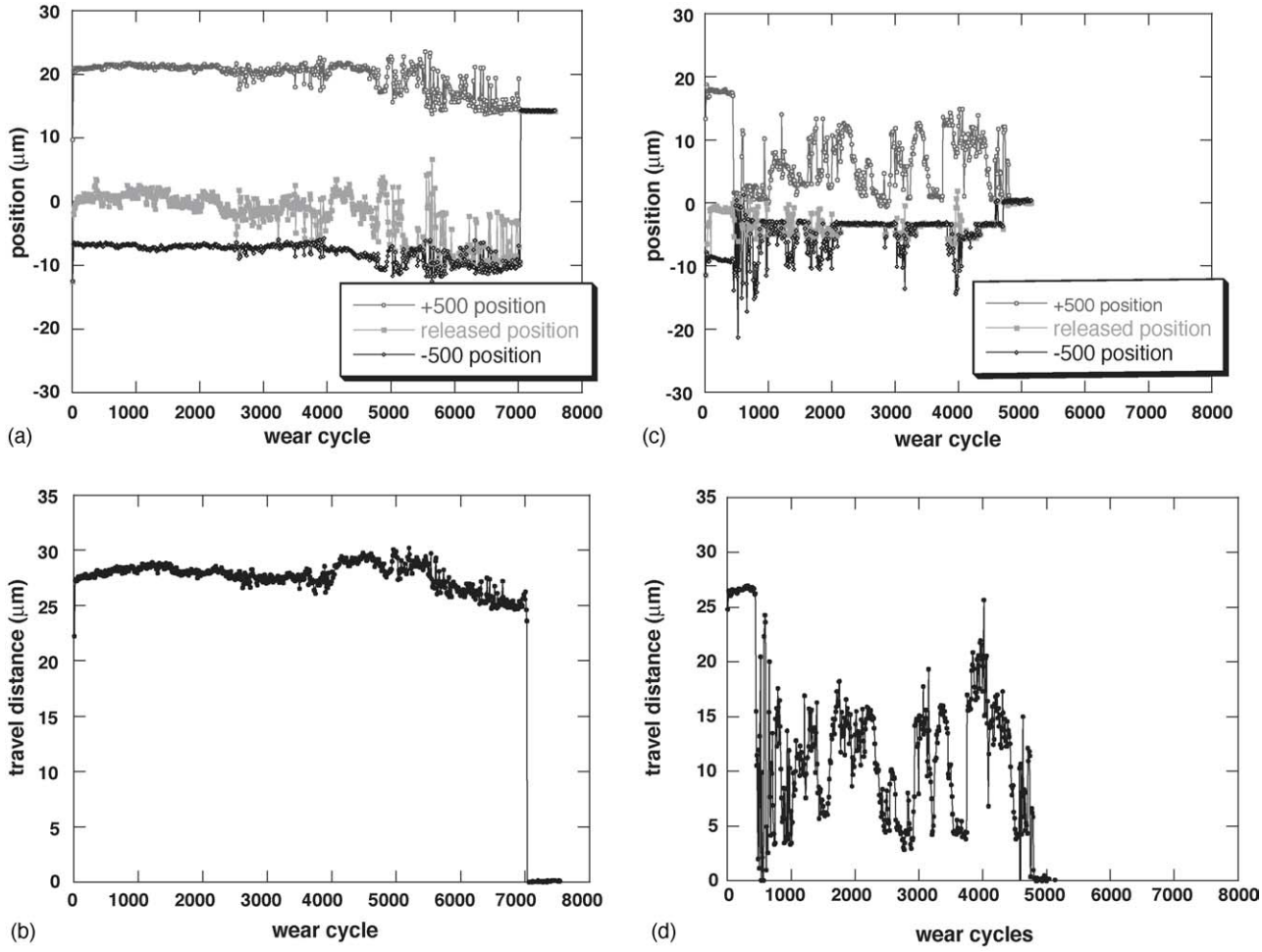

Fig. 8. Representative nanotractor performance during a wear test. (a) Positions of the nanotractor during the wear test for a device from Lot A, which received CMP on P0 after deposition. Every 10th cycle, the position is recorded after walking out 500 steps (+500 position), after returning 500 steps (−500 position) and after the clamp voltages are set to zero (released position). (b) Travel distance of the nanotractor every 10 cycles during the wear test for the same device as in (a). The travel distance is defined as the difference between the +500 and −500 positions. Variation in the travel distance only increases slightly before stiction failure at around 7000 cycles. (c) Positions of the nanotractor recorded every 10 cycles during the wear test, as in (a), for an oxide-coated device from Lot B. (d) Travel distance of the nanotractor during the wear test every 10 cycles, as in (b), for the same device as in (c). The distance traveled by the nanotractor varies more from cycle to cycle for the oxide-coated surface than for the monolayer-coated one (compare to b).

5700 cycles), the released nanotractor is intermittently found on the positive side of zero. In these cases, it appears that the nanotractor was released with enough momentum to reach the other side of zero and remained adhered there. For the case of Fig. 8(a), during the period between cycles 5200 and 5400, the nanotractor tends to stay very close to the −500 position after the loads are released, instead of returning to its zero position. This indicates that the static friction due to adhesive loading increased due to surface wear. Just before failure at 7000 cycles, there is significant variation in all three positions. Finally all three positions suddenly become equivalent when the nanotractor becomes permanently lodged at about three-fourths of its initial maximum walking distance.

Fig. 8(b) shows the travel distance of the nanotractor every tenth wear cycle, as calculated by taking the difference in position when walked out (+500 steps) and walked in (−500 steps). The nanotractor travel distance decreases slightly before failure, and when the device fails, the travel distance abruptly becomes zero.

Table 1 also gives the number of cycles to failure for each device that was tested. From the limited number of tested performed, there is no significant difference in wear behavior between the samples of differing roughness in Lot A. Most of the devices failed between 5000 and 8000 cycles, with one exceptional case of an extremely short-lived device that failed after 2700 cycles. However, the results from Lot B indicate a significant difference in behavior between monolayer-coated and oxide-coated device surfaces, whereby both oxide-coated surfaces fail before 5000 cycles. Data from a wear test on a Lot B oxide-coated sample is shown in Fig. 8(c) and (d) for comparison to results on a Lot A monolayer-coated sample in (a) and (b). The travel distance of the oxide-coated nanotractor (Fig. 8(d)) varies from cycle to cycle much earlier and more frequently than the monolayer-coated nanotractor

(Fig. 8(b)). It can also be seen that the oxide-coated nanotractor behaves reliably for only a fraction of its wear lifetime, after which the travel distance is very inconsistent. This behavior proceeds until stiction failure occurs at approximately 4800 wear cycles for the oxide-coated device. Although the other oxide-coated device tested in this study continued to operate for several thousand cycles (see Table 1), its travel distance as a function of the number of wear cycles is characteristically similar to the behavior seen in Fig. 8(c) and (d). Therefore, we find that, for devices that have not received any additional roughening treatment, there is a significant reduction in the quality of operation of the oxide-coated devices compared to the monolayer-coated devices.

5.2. AFM imaging of the wear track

After a wear test is performed on a nanotractor device, the induced wear track on the sample surfaces, which extends beyond the at-rest nanotractor position, can be imaged using AFM or SEM. The final resting position of a nanotractor after a test often allows sufficient clearance for a scanning AFM tip. An SEM image of such a region, including the wear track, is shown in Fig. 9. Fig. 10 shows a representative pair of intermittent-contact mode AFM images of a wear track on another nanotractor device surface. In this case, the surface imaging was performed using the Nanoscope IIIa Dimension 5000 AFM. This image was taken of a 6 μm by 6 μm region of the surface of a Lot A sample, which received the nominal wafer processing and a monolayer coating.

It can be seen that the worn and unworn regions are clearly demarcated from each other in both the topography (Fig. 10(a)) and phase images (Fig. 10(b)), which were acquired simultaneously and reveal a 1 μm-wide wear track. We know that the friction counterface is 2 μm wide (see Fig. 3(b) and (c)), so this discrepancy may be due to a slight curvature in the friction counterface that is not noticeable in the SEM shown in Fig. 3(c). In this case, the stress under the slider is non-uniform and more concentrated toward the center of the wear track, producing more wear in that region. The wear varies along the length of the track, producing grooves as seen in Fig. 10, and regions where debris pileup occurred. Because of the complex nature of the surface interactions we could not estimate the wear volume and use a simple 'Archard wear law' to determine a wear coefficient. This requires a more detailed analysis of the surface topographies of both the substrate and the countersurface over large regions of the affected surface, which will be provided in-depth in a future publication.

In the phase image, there is a distinct contrast between the worn and unworn regions, which will be discussed further below, and in a future publication. The phase contrast between these two regions cannot be attributed solely to topographic variation, since this would only cause phase contrast corre-

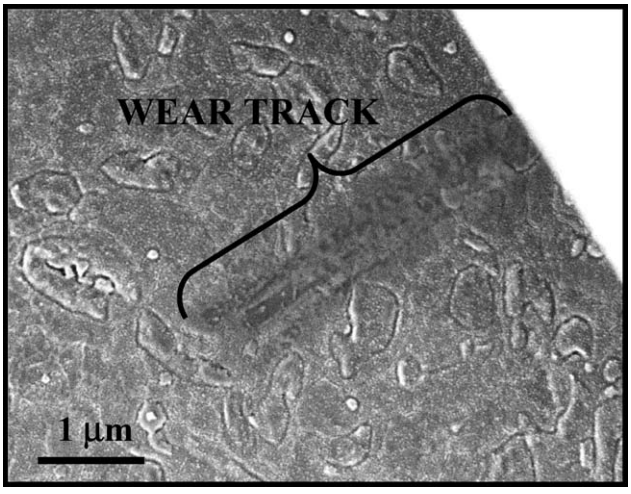

Fig. 9. SEM image of a wear track. The image was taken at normal incidence to the sample. This wear track extends beyond the at-rest nanotractor seen in the upper right corner of this image (white triangular area). The region of this image is located at the far right end of the nanotractor as shown in Fig. 3a. The extension of the wear track past the nanotractor allows for AFM imaging without destruction of the nanotractor device. This sample is from Lot A and received the nominal wafer processing.

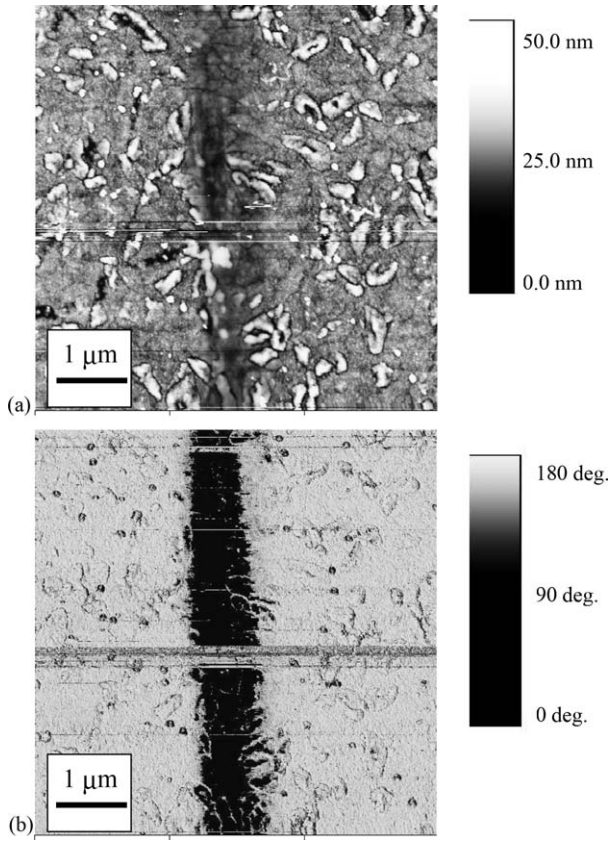

Fig. 10. AFM intermittent contact mode images of another nanotractor wear track. This sample is from Lot A and received the nominal wafer processing, but is a different device from the one shown in Fig. 9. (a) Surface topography clearly shows height and morphology differences in worn and unworn regions of the sample surface. (b) The phase image, captured simultaneously with the topography information, also shows a distinction between worn and unworn regions. This contrast may be due to chemical/structural changes of the monolayer and/or the polysilicon surface.

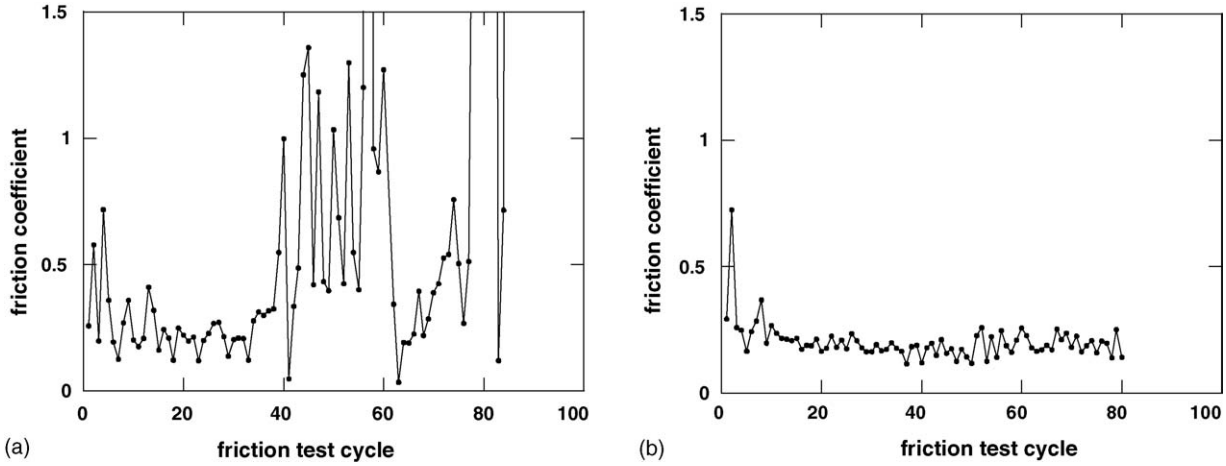

Fig. 11. Variation of friction coefficient with number of friction tests performed for two samples from Lot A. (a) Friction coefficient for an oxide-coated surface from Lot A. (b) Friction coefficient for a monolayer-coated surface from Lot A.

sponding to changes in surface slope, e.g. on the edges of the wear track. Also note that the streaks in both topography and phase images were a common phenomenon when imaging the wear track region of the sample.

5.3. Friction tests

The behavior of an oxide-coated sample and a monolayer-coated sample measured via friction tests are shown in Fig. 11(a) and (b), respectively. Because the friction test involves sliding under much higher normal loads (106 μN), it is not expected that the nanotractor should survive for as many cycles as in the wear test. Indeed, after approximately 80 friction tests were performed on an oxide-coated surface, the device failed due to wear (Fig. 11(a)). However, a monolayer-coated device survived 80 friction test cycles with no apparent change in friction coefficient (Fig. 11(b)) and without failure. For the oxide-coated surface, the friction coefficient initially shows moderate variation for the first ∼35 test cycles (0.25 ± 0.12), but eventually it starts to vary substantially. The device with monolayer-coated surfaces, on the other hand, produces more consistent friction coefficient values (0.19 ± 0.04) and survives much longer. For both the monolayer-coated and oxide-coated surfaces, there is an initial spike in the friction coefficient that may be related to the initial removal of hydrocarbons from the surface, or the initial wear of the sharpest, tallest asperities in the contact.

5.4. Friction and wear tests

Given that during the friction test the friction coefficient does not change substantially over just a few cycles, friction tests and wear tests were performed in sequence to determine the progressive change of the friction coefficient with increasing wear. The tests were performed in the following sequence: 20 friction test cycles, followed by 1000 wear test cycles, repeated until failure. Fig. 12 shows one such collection of tests, conducted on a sample from Lot A (100 min oxidation). The average friction coefficient and its cycle-to-cycle variation increase with each successive repetition of wear test cycles. The travel distance is mostly unaffected by the intermediate friction tests. Only very close to failure is there any deviation in the nanotractor travel distance (Fig. 12(a)).

The average friction coefficient for each set of 20 friction tests is shown as a function of the number of wear tests for devices from Lots A and B in Fig. 13. The friction coefficient tends to increase with wear, as seen in Fig. 12. This shows that the nanotractor becomes much less reliable as the number of wear cycles increases, as was also observed in the wear tests. It also shows that the friction coefficient is a more sensitive indicator of damage and progression toward failure than the measurement of travel distance.

6. Discussion

These preliminary tests provide information about friction and wear properties of polysilicon MEMS surfaces in a well-controlled sliding environment. The data clearly show that performance is greatly enhanced by a monolayer coating. It is not yet clear whether surface roughness has any effect on the tribological behavior of these surfaces. Many more tests need to be performed to achieve statistically significant results on wear lifetime with respect to different surface treatments.

Variations in friction occur long before total failure of the device, even while the total distance traveled remains nearly the same. This indicates that the friction coefficient between components of a MEMS device is a much more sensitive test of the state of the device's surfaces than the actual displacement that occurs. Simply observing the displacement of a device may not provide sufficient, if any, insight into how

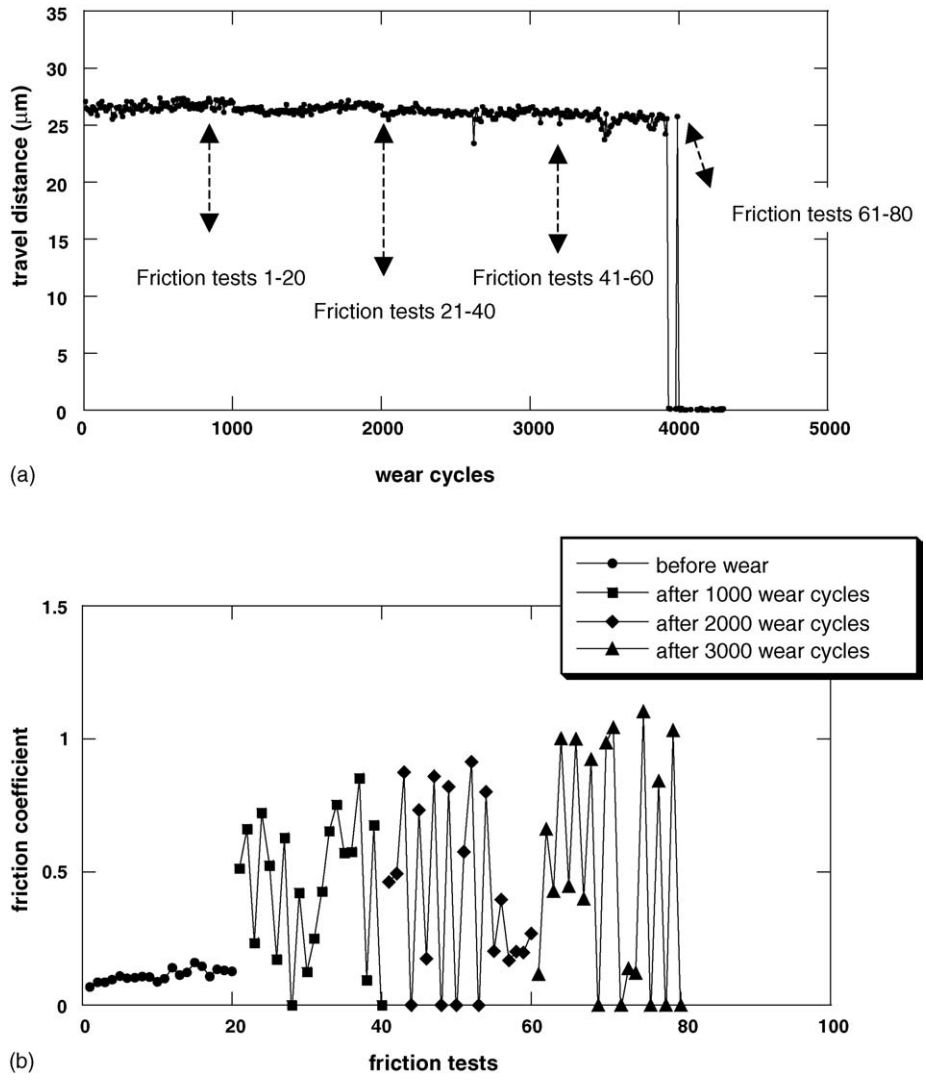

Fig. 12. A representative friction and wear test. 20 friction tests cycles are followed by then 1000 wear cycles, and then repeated until failure. Data are from a test performed on a Lot A sample that received 300 min oxidation. (a) Travel distance of the nanotractor during the wear test every 10 cycles, as in Fig. 7. The arrows indicate that after each set of 1000 wear cycles, 20 friction test cycles are performed. (b) Friction coefficient as calculated between each set of wear tests. The friction coefficient and its variation both increase with each successive set of friction tests.

close the device is to failure. This implies that any in situ predictive diagnostic approach should take this into account.

Several possible improvements in the testing procedures are evident. In particular, the restraint on the movement of the nanotractor by load spring B particularly at the most extended position, may have lead to severe wearing of the surface and of the nanotractor rail itself. Our AFM studies thus far have indeed shown a corresponding inhomogeneity in the wear track. Sliding is exacerbated locally at the maximum position at +500 steps, inducing non-uniform wear along the sliding track. For future testing, the walking distance of the nanotractor can be modified so that the nanotractor does not reach its maximum force during its travel in a wear test. Alternatively, we can examine the wear tracks on the side of the clamp that is closer to the actuation plate. Here, the wear will be directly related to the number of cycles.

The phase signal recorded during intermittent-contact AFM imaging shows contrast between the worn and unworn regions of the polysilicon surface, as seen in Fig. 10(b) for a monolayer-coated device from Lot A, with the nominal processing. This was observed for both monolayer-coated and oxide-coated surfaces. The phase signal gives information about the chemical nature and structure of the material, both in-plane and out-of-plane [39,44]. In our case, the phase contrast indicates modification either to the monolayer or to the polysilicon itself. It has been previously observed that repeated sliding over a monolayer causes modification in its frictional response [45–47]. It is possible that the local arrangement or bonding of the fluorocarbon chains has been altered, or that the monolayer has been removed due to multiple cycles of sliding. The scan line streaks noted above further support the idea that modification of the monolayer has

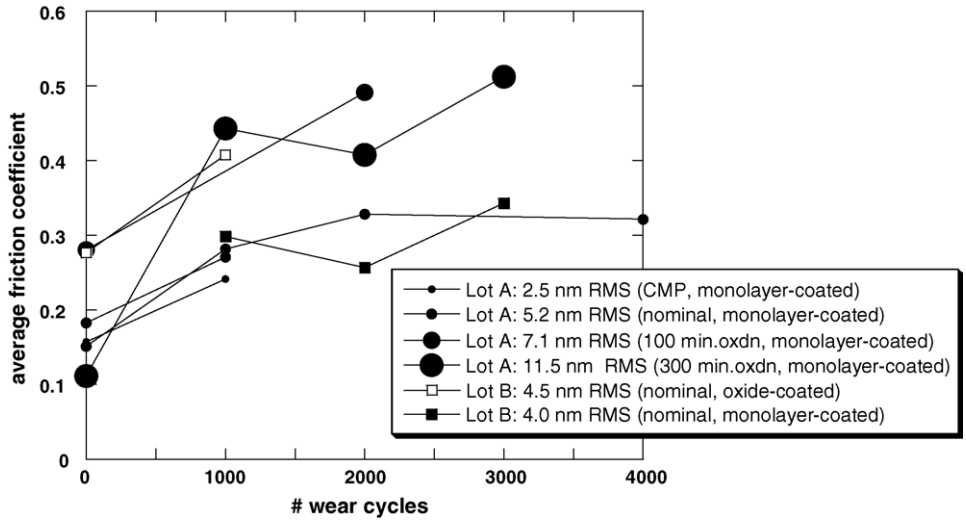

Fig. 13. Comparison of friction coefficient as a function of wear cycles for the various samples. The size of the data points signifies the relative roughness of each sample, as also indicated in the figure legend.

occurred, since loose fluorocarbon molecules could cause a transient instability between the tip and the surface that hinders the tracking of the tip across the surface to create this artifact. In any event, since phase contrast is observed between worn and unworn regions of the oxide-coated surface, it is possible that polysilicon itself is being modified due to wear or even due to a phase transformation. Further study of the fundamental mechanisms of wear using spatially-resolved spectroscopic tools is currently under way.

7. Concluding remarks/future work

The work performed thus far indicates that the nanotractor is a promising vehicle for in situ wear studies on MEMS devices. Although more experiments are needed and further development of the testing methodology is required, several conclusions can be made. First, the nanotractor device fails via interfacial seizure due to wear processes at the sliding interfaces under well-characterized loading conditions. Although it is necessary to develop more sensitive in situ tests, this is a necessary observation to justify the further development of nanotractor wear tests. Second, the tests were conducted under 44 kPa apparent pressure, and noticeable wear of the polysilicon surface was observed. With this device, it should be possible to study the onset of wear as a function of lighter loading conditions. Third, a monolayer lubricant of FOTAS significantly enhances the wear resistance of MEMS surfaces. Fourth, surface roughness does not strongly affect wear properties, based on the limited number of measurements so far. Fifth, as long as only a limited amount of friction testing is conducted, we can directly measure the friction coefficient as a function of wear. It is possible to measure friction for monolayer-coated surfaces, since little change with number of friction tests cycles is observed. For the oxide-coated surfaces, friction tests should be performed at lower loads to reduce wear during the friction test. Sixth, the friction coefficient can vary substantially long before failure and before device performance (such as travel distance) is altered. Finally, AFM can be applied to study surface modification without dissembling the nanotractor device, because of the large travel distances (>20 μm) that the nanotractor undergoes during a wear test, leaving an exposed wear track on the PO layer for investigation. Therefore, in future studies it should be possible to conduct wear and AFM tests sequentially on the same device to follow the evolving topography.

All of these results are important for the understanding of MEMS device reliability. We have shown that this unique, in situ method is highly revealing and holds promise for developing a more quantitative and predictive understanding of MEMS device reliability.

Acknowledgements

We acknowledge the staff at the Microelectronics Development Laboratory at Sandia National Laboratories for fabricating the samples, and in particular Michael J. Shaw for the processing of the Lot A splits. We also acknowledge contributions of Mark D. Street for AFM investigations of wear track topography and determination of wafer roughnesses via AFM, and David S. Grierson for the SEM image of the nanotractor wear track. This work was supported by the US Department of Energy, BES-Materials Sciences, under Contract DE-FG02-02ER46016, and by Sandia National Laboratories. Sandia is a multiprogram laboratory operated by Sandia Corporation, a Lockheed Martin Company, for the United States

Department of Energy's National Nuclear Security Administration under Contract DE-AC04-94AL85000. We also acknowledge partial support from the DOE/BES Center for Excellence in Nanotribology.

References

[1] K.H.L. Chau, R.E. Sulouff, Technology for the high-volume manufacturing of integrated surface-micromachined accelerometer products, Microelectron. J. 29 (1998) 579–586.
[2] R. Frank, Pressure sensors merge micromachining and microelectronics, Sens. Actuators A 28 (1991) 93–103.
[3] S.A. Henck, Lubrication of digital micromirrordevices™, Tribol. Lett. 3 (1997) 239–247.
[4] P.F. van Kessel, L.J. Hornbeck, R.E. Meier, M.R. Douglass, MEMS based projection display, Proc. IEEE (1998).
[5] J.J. Sniegowski, E.J. Garcia, Microfabricated actuators and their application to optics, in: Miniaturized Systems with Micro-Optics and Micromechanics, San Jose, CA, 1995.
[6] J.J. Sniegowski, S.L. Miller, G.F. LaVigne, M.S. Rodgers, P.J. McWhorter, Monolithic geared mechanisms driven by a polysilicon surface-micromachined on-chip electrostatric microengine, Solid-State Sensor and Actuator Workshop, Transducers Research Foundation, Hilton Head Island, South Carolina, June 3–6, 1996.
[7] S.M. Barnes, S.L. Miller, M.S. Rodgers, F. Bitsie, Torsional ratcheting actuating system, in: Proceedings of the Third International Conference on Modeling and Simulation of Microsystems, San Diego, CA, 2000.
[8] J.J. Allen, H.K. Schriner, Micromachine wedge stepping motor, in: ASME IMECE, ASME International, Anaheim, CA, 1998.
[9] R. Yeh, S. Hollar, K.S.J. Pister, Single mask, large force, and large displacement electrostatic linear inchworm motors, J. Microelectromech. Syst. 11 (2002) 330–336.
[10] J.J. Sniegowski, M.P. de Boer, IC-compatible polysilicon surface micromachining, Annu. Rev. Mater. Sci. 30 (2000) 299–333.
[11] J. Yang, H. Kahn, A.Q. He, S.M. Phillips, H. Heuer, A new technique for producing large-area as-deposited zero-stress LPCVD polysilicon films: The MultiPoly process, J. Microelectromech. Syst. 9 (2000) 485–494.
[12] M.S. Baker, M.P. de Boer, N.F. Smith, L.K. Warne, M.B. Sinclair, Integrated measurement-modeling approaches for evaluating residual stress using micromachined fixed-fixed beams, J. Microelectromech. Syst. 11 (2002) 743–753.
[13] B.D. Jensen, M.P. de Boer, N.D. Masters, F. Bitsie, D.A. LaVan, Interferometry of actuated cantilevers to determine material properties and test structure nonidealities in MEMS, J. Microelectromech. Syst. 10 (2001) 336–346.
[14] R. Ballarini, H. Kahn, N. Tyebi, A.H. Heuer, Effect of microstructure on the strength and fracture toughness of polysilicon, in: Mechanical Properties of Structural Thin Films, ASTM, West Conshohocken, PA, 2001.
[15] J. Bagdahn, W.N. Sharpe, O. Jadaan, Fracture strength of polysilicon at stress concentrations, J. Microelectromech. Syst. 12 (2003) 302–312.
[16] A.D. Romig, M.T. Dugger, P.J. McWhorter, Materials issues in microelectromechanical devices: science, engineering, manufacturability and reliability, Acta Mat. 51 (2003) 5837–5866.
[17] M. Mehregany, K.J. Gabriel, W.S.N. Trimmer, Integrated fabrication of polysilicon mechanisms, IEEE Trans. Electron Devices 35 (1988) 719–723.
[18] K.J. Gabriel, F. Behi, R. Mahadevan, M. Mehregany, In situ friction and wear measurements in integrated polysilicon mechanisms, Sens. Actuators A 21 (1990) 184–188.
[19] Y.C. Tai, R.S. Muller, IC-processed electrostatic synchronous micromotors, Sens. Actuators A 20 (1989) 49–55.
[20] Y.C. Tai, R.S. Muller, Frictional study of IC-processed micromotors, Sens. Actuators A 21 (1990) 180–183.
[21] M.G. Lim, J.C. Chang, D.P. Schultz, R.T. Howe, R.M. White, Polysilicon microstructures to characterize static friction, in: Proceedings of IEEE Third MEMS Workshop, Napa Valley, CA, 1990.
[22] U. Beerschwinger, D. Mathieson, R.L. Reuben, S.J. Yang, A study of wear on MEMS contact morphologies, J. Micromech. Microeng. 4 (1994) 95–105.
[23] U. Beerschwinger, R.L. Reuben, S.J. Yang, Frictional study of micromotor bearings, Sens. Actuators A 63 (1997) 229–241.
[24] G.T. Mulnern, D.S. Soane, R.T. Howe, Supercritical carbon dioxide drying of microstructures, in: Proceedings of the Seventh International Conference on Solid State Sensors and Actuators, Transducers' 93, Yokohama, Japan, 1993.
[25] U. Srinivasan, J.D. Foster, U. Habib, R.T. Howe, R. Maboudian, D.C. Senft, M.T. Dugger, Lubrication of polysilicon micromechanisms with self-assembled monolayers. Hilton Head 98, Hilton Head Island, SC, USA, 1998.
[26] W.R. Ashurst, C. Yau, C. Carraro, C. Lee, R.T. Howe, R. Maboudian, Alkene based monolayer films as anti-stiction coatings for polysilicon MEMS, Sens. Actuators A 9 (2001) 239–248.
[27] T.M. Mayer, M.P. de Boer, N.D. Shinn, P.J. Clews, T.A. Michalske, Chemical vapor deposition of fluoroalkylsilane monolayer films for adhesion control in microelectromechanical systems, J. Vac. Sci. Technol. B 18 (2000) 2433–2440.
[28] J.J. Sniegowski, E.J. Garcia, Surface-micromachined gear trains driven by an on-chip electrostatic microengine, IEEE Electron Device Lett. 17 (1996) 366–368.
[29] S.L. Miller, J.J. Sniegowski, G. LaVigne, P.J. McWhorter, Performance tradeoffs for a surface micromachined microengine, Proc. SPIE: Int. Soc. Opt. Eng. 2882 (1996) 182–191.
[30] D.M. Tanner, M.T. Dugger, Wear mechanisms in reliability methodology, Proc. SPIE: Int. Soc. Opt. Eng. 4980 (2003) 22–40.
[31] A.B. Mann, D. van Heerden, J.B. Pethica, T.P. Weihs, Size-dependent phase transformations during point loading of silicon, J. Mater. Res. 15 (2000) 1754–1758.
[32] B. Bhushan, X.D. Li, Micromechanical and tribological characterization of doped single-crystal silicon and polysilicon films for microelectromechanical systems devices, J. Mater. Res. 12 (1997) 54–63.
[33] S. Sundararajan, B. Bhushan, Micro/nanotribological studies of polysilicon and SiC films for MEMS applications, Wear 217 (1998) 251–261.
[34] M.P. de Boer, D.L. Luck, W.R. Ashurst, R. Maboudian, A.D. Corwin, J.A. Walraven, J.M. Redmond, High performance surface micromachined inchworm actuator, J. Microelectromech. Syst. 13 (2004) 63–74.
[35] A.D. Corwin, M.P. de Boer, Effect of adhesion on dynamic and static friction in surface micromachining, Appl. Phys. Lett. 84 (2004) 2451–2453.
[36] W.C. Young, Roark's Formulas for Stress and Strain, sixth ed., McGraw-Hill, New York, 1989, p. 650.
[37] K.-T. Wan, B.R. Lawn, R.G. Horn, Repulsive interaction between coplanar cracks in the double cantilever geometry, J. Mater. Res. 7 (1992) 1584–1588.
[39] R. Garcia, R. Perez, Dynamic atomic force microscopy methods, Surf. Sci. Rep. 47 (2002) 197–301.
[40] M.G. Hankins, P.J. Resnick, P.J. Clews, T.M. Mayer, D.R. Wheeler, D.M. Tanner, R.A. Plass, Vapor deposition of amino-functionalized self-assembled monolayers on MEMS, Proc. SPIE 4980 (2003) 189–196.
[41] P.J. Resnick, P.J. Clews, Whole wafer critical point drying of MEMS devices, in: Reliability, Testing and Characterization of MEMS/MOEMS, San Francisco, CA, 2001.

[43] D.L. Luck, M.P. de Boer, W.R. Ashurst, M.S. Baker, Evidence for presliding tangential deflections in MEMS friction, Transducers 2003, Boston, 2003.
[44] M.S. Marcus, R.W. Carpick, D.Y. Sasaki, M.A. Eriksson, Material anisotropy revealed by phase contrast in intermittent contact atomic force microscopy, Phys. Rev. Lett. 88 (2002), 226103/1-4.
[45] L.M. Qian, X.D. Xiao, S.Z. Wen, Tip in situ chemical modification and its effects on tribological measurements, Langmuir 16 (2000) 662–670.
[46] J.D. Kiely, J.E. Houston, Contact hysteresis and friction of alkanethiol self-assembled monolayers on gold, Langmuir 15 (1999) 4513–4519.
[47] J.D. Kiely, J.E. Houston, J.A. Mulder, R.P. Hsung, X.Y. Zhu, Adhesion, deformation and friction for self-assembled monolayers on Au and Si surfaces, Tribol. Lett. 7 (1999) 103–107.